Journal of Computational Neuroscience (2019) 46:3–17
https://doi.org/10.1007/s10827-018-0705-9

An exploratory data analysis method for identifying brain regions and frequencies of interest from large-scale neural recordings

Macauley S. Breault[1] · **Pierre Sacré**[1] · **Jorge González-Martínez**[2] · **John T. Gale**[3] · **Sridevi V. Sarma**[1]

Received: 17 January 2018 / Revised: 28 August 2018 / Accepted: 23 October 2018 / Published online: 4 December 2018

Abstract

High-resolution whole brain recordings have the potential to uncover unknown functionality but also present the challenge of how to find such associations between brain and behavior when presented with a large number of regions and spectral frequencies. In this paper, we propose an exploratory data analysis method that sorts through a massive quantity of multivariate neural recordings to quickly extract a subset of brain regions and frequencies that encode behavior. This approach combines existing tools and exploits low-rank approximation of matrices without *a priori* selection of regions and frequency bands for analysis. In detail, the spectral content of neural activity across all frequencies of each recording contact is computed and represented as a matrix. Then, the rank-1 approximation of the matrix is computed using singular value decomposition and the associated singular vectors are extracted. The temporal singular vector, which captures the salient features of the spectrogram, is then correlated to the trial-varying behavioral signal. The distribution of correlations for each brain region is efficiently computed and used to find a subset of regions and frequency bands of interest for further examination. As an illustration, we apply this approach to a data set of local field potentials collected using stereoelectroencephalography from a human subject performing a reaching task. Using the proposed procedure, we produced a comprehensive set of brain regions and frequencies related to our specific behavior. We demonstrate how this tool can produce preliminary results that capture neural patterns related to behavior and aid in formulating data-driven hypotheses, hence reducing the time it takes for any scientist to transition from the exploratory to the confirmatory phase.

Keywords Exploratory data analysis · Multivariate neural data · Singular value decomposition · Stereoelectroencephalography

1 Introduction

The BRAIN Initiative has led to the emergence of new neurotechnologies that probe and manipulate the brain at multiple scales, from cells to systems at fine temporal resolution. Availability of these new data has, in turn, led to the emergence of a new field of neuroscience that is computational and data-intensive. In the past, the knowledge about the brain was limited by the fact that the necessary data were simply not available (Cunningham and Yu 2014). In the future, the huge amount of available data will be more of a problem than its previous scarcity. Just as technological advancements have fluctuated the capacity of data availability and computational power, the approaches used to analyze these large multivariate neural data sets must scale to meet demand (Brown et al. 2004).

It is now more common than ever to come across large-scale high temporal resolution, whole brain recordings from humans and nonhuman primates obtained using techniques such as ElectroEncephaloGraphy (EEG), ElectroCorticoGraphy (ECoG), Stereo-EEG (SEEG), and Magneto-EEG (MEG). Neuroscientists often investigate the spectral content of continuous neural signals obtained using these techniques as

Action Editor: Genevera Allen

✉ Macauley S. Breault
mbreaul1@jhu.edu

Sridevi V. Sarma
ssarma2@jhu.edu

[1] Department of Biomedical Engineering, Johns Hopkins University, Baltimore, MD 21218, USA

[2] Center for Epilepsy, Cleveland Clinic, Cleveland, OH 44195, USA

[3] Department of Neurosurgery, Emory University, Atlanta, GA 30322, USA

the power in specific frequency bands. These are shown to play important roles in encoding and communicating information about the environment at a population-level (Ward 2003). For example, beta band oscillations are found throughout motor regions of the brain and, when present, are thought to block movement initiation, while the gamma band is thought to facilitate movement (Crone et al. 1998a, b). Theta band oscillations play an important role in learning and memory (Kahana et al. 2001), REM sleep (Jouvet 1969; Kahana et al. 2001), and arousal (Basar et al. 2000). But could there be something more?

The magnitude of neural data collected from experiments makes it difficult to find meaningful information out of their inherent subtle and complex patterns. To reduce its dimensionality, investigators typically limit the scope of their analysis to a specific subset of brain regions and frequency bands in recorded brain signals, thus ignoring a large chunk of their data (Crone et al. 1998a, b). Another common trimming approach is to average neural activity across multiple trials, eliminating temporal variation that could have provided interesting insight (Breault et al. 2017; Cunningham and Yu 2014; Kerr et al. 2014). An ideal data mining approach would extract possible underlying trends in the neural data related to behavioral measurements without predefining constraints such as regions or frequencies.

In particular, it would be highly useful to have a single exploratory data analysis tool that (i) processes the entire data set at once—all regions and frequencies—and then (ii) generates a rank order list of regions and frequencies of interest (iii) without necessarily being guided by a predefined hypothesis. This would then be followed by confirmatory data analysis, where the significance of correlations between brain and behavior is quantified. In principle, this method should quickly extract neural correlates using any dynamic signal, such as behavior, without requiring *a priori* knowledge of which brain regions nor frequency band to study. It should also preserve the dynamic nature of the neural activity related to temporal brain processes yet be flexible enough to allow for trial-to-trial variability (Cunningham and Yu 2014; Ward 2003).

We propose a method, in the form of a tool, that uses Singular Value Decomposition (SVD) and its low-rank matrix approximation to identify neural correlates of behavior from whole brain recordings which meets the above requirements. Specifically, the method involves computing spectrograms over time windows of interest for each brain region and trial—viewing the spectrograms as rectangular matrices, where columns represent frequency bins (e.g., ranging from 1–200 Hz), rows represent time bins, and cell values represent power in a given frequency and time bin. SVD is then performed on each matrix to compute its rank-1 approximation matrix, which corresponds to the largest singular value and associated singular vectors. Optionally, multiple matrices can be found using the other singular components to extract other characteristics from the original spectrogram. For each approximation, we extract the left or *temporal singular vector*. This vector is a temporal signal that retains important characteristics of how the spectral content across *all* frequencies evolves over the time window. The temporal singular vector is then correlated to the behavioral signal using cross-correlation for each brain region and trial (Varela et al. 2001). These correlation statistics can then be rigorously analyzed—within brain regions, across trials, and subjects—to generate a ranked list of regions and frequencies of interest.

The use of SVD on neuronal data is not novel. Similar to SVD, Principal Components Analysis (PCA) is a technique widely used in neuroscience to cluster individual neurons into populations based on similar activity (D'Aleo et al. 2017; Lewicki 1998), reduce dimensionality of neuronal signals (Agarwal et al. 2015; Cunningham and Yu 2014), control Brain–Computer Interfaces (Chapin 2004), and even localize brain activity or extract features from EEG data (Cong et al. 2015). However, unlike traditional applications, which use PCA for grouping, we are using it to study the dominant modes (time and frequency) in spectral data.

We demonstrate the use of this tool on data collected from a motor control experiment, wherein SEEG neural recordings were acquired from one epilepsy human subject undergoing invasive monitoring at the Cleveland Clinic for treatment purposes. The data set consisted of Local Field Potential (LFP) recordings from 62 electrode contacts across 24 unique, nonmotor brain regions while the subject performed 98 trials of a center-out arm reaching task. The breadth of access and originality provided by this study was met with the daunting task of sifting through this large data set of neuronal activities in hopes of finding neural correlates of movement. Since all electrode contacts were in nonmotor regions, there was no clear hypothesis as to which regions and frequency bands are of interest. Our goal was to determine whether nonmotor regions encode path-related information, and in particular, we were interested in whether the activity in any of these regions modulates with the temporal evolution of movement in a consistent manner.

2 Methods

In this section, we describe our proposed exploratory data analysis tool that processes large-scale neural data to establish a finite set of brain regions and frequencies that correlate to behavior. An outline of this procedure is illustrated in Fig. 1a.

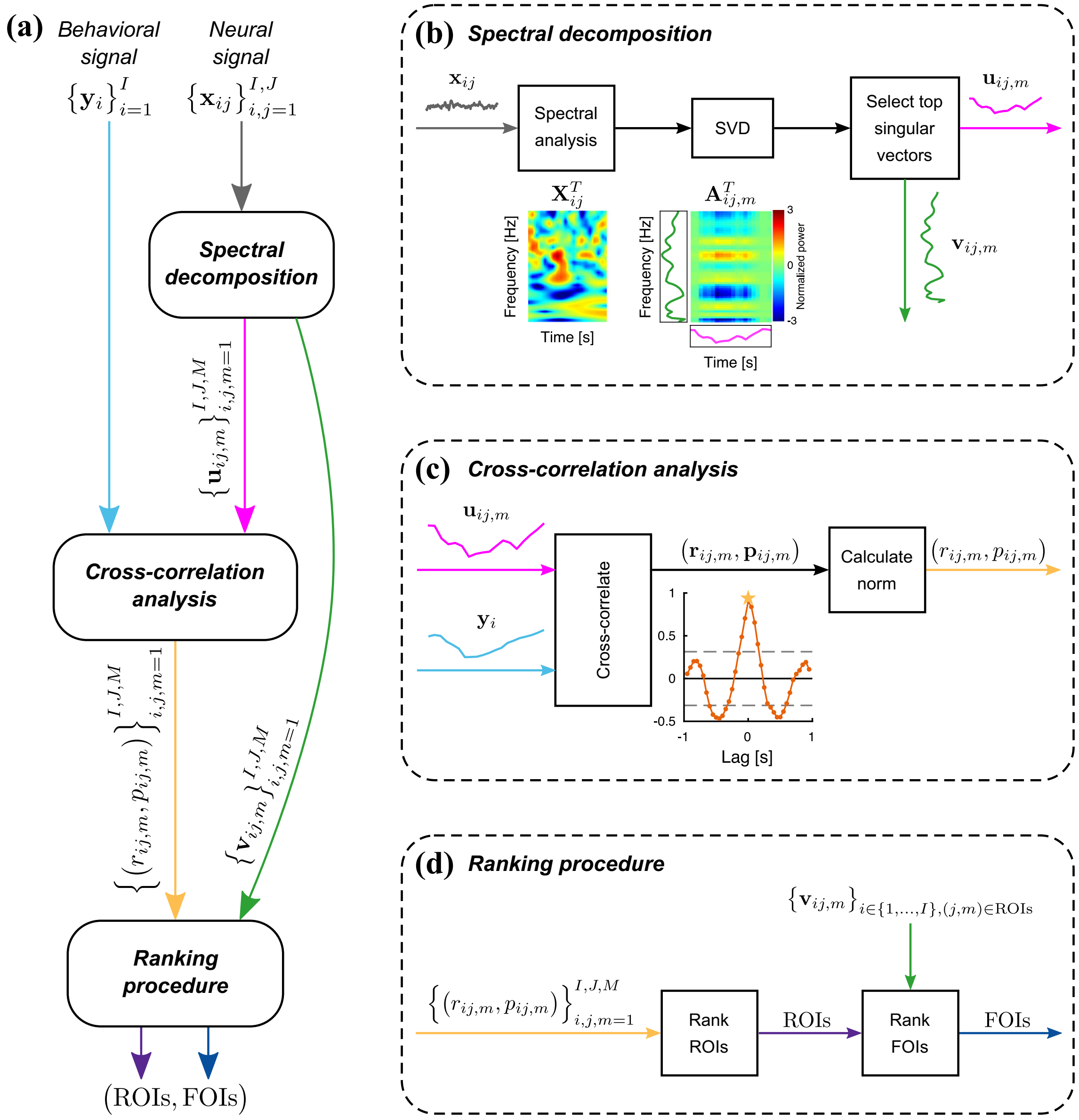

Fig. 1 **a** The overall architecture of the proposed analysis for all brain regions $j = 1, ..., J$ and trials $i = 1, ..., I$. This method takes in the neural signal $\mathbf{x}_{ij}$ and the behavioral signal $\mathbf{y}_i$ to extract Regions-Of-Interest (ROIs) and corresponding Frequencies-Of-Interest (FOIs). It is broken down into three general steps. **b** *Spectral Decomposition*. For brain region j and trial i, the raw neural signal of voltage over time $\mathbf{x}_{ij}$ is transformed into its time-frequency representation through spectral methods to produce a spectrogram $\mathbf{X}_{ij}$. This matrix is then broken down using SVD to find the top modes, denoted $\mathbf{A}_{ij,m}$. The output of this step is the temporal singular vector $\mathbf{u}_{ij,1}$ associated with the time domain of $\mathbf{A}_{ij,m}$ and the frequency singular vector $\mathbf{v}_{ij,m}$ associated with the frequency domain of $\mathbf{A}_{ij,m}$, which is used in a later step. **c** *Cross-correlation analysis*. The behavioral signal $\mathbf{y}_i$ and $\mathbf{u}_{ij,m}$ are cross-correlated to produce a range of correlations, denoted $\mathbf{r}_{ij,m}$, as a function of lag between the two signals with the 95%-confidence interval (dashed line) and associated p-values, denoted $\mathbf{p}_{ij,m}$. The infinity norm of $\mathbf{r}_{ij,m}$ is calculated as $r_{ij,m}$. The p-value at the lag of the infinity norm is saved as $p_{ij,m}$. **d** *Ranking procedure*. The process of creating a rank ordered list begins by finding the ROIs across all trials, brain regions, and modes. An average correlation $\overline{r}_{j,m}$ and p-value $\overline{p}_{j,m}$ are calculated for each brain region using the output metrics from the previous step across all trials. The list of ROIs is found by sorting $\overline{r}_{j,m}$ or $\overline{p}_{j,m}$. A subset can be obtained by applying a threshold to $\overline{r}_{j,m}$ or $\overline{p}_{j,m}$ to distinguish ROIs that are very correlated from not very correlated. To find the FOIs for each ROIs, $\mathbf{v}_{ij,m}$ is averaged over all trials per region. Then, the frequency bins of $\overline{\mathbf{v}}_{j,m}$ are sorted to produce a list from highest to lowest average frequency singular value. Similarly, FOIs in terms of bands are calculated by averaging the aggregation of $\overline{\mathbf{v}}_{j,m}$ into each frequency band, based on predefined frequency bounds. In the end, this analysis produces a data-driven list or subset of ROIs and FOIs

2.1 Notation

This method applies to data sets that contain recordings from multiple brain regions indexed by $j \in \{1, \ldots, J\}$ and multiple repeated samples of structured behavior that can be partitioned into trials indexed by $i \in \{1, \ldots, I\}$.

Let $x_{ij}(t) \in \mathbb{R}$ be the continuous signal of time-varying neural activity recorded from brain region j during trial i. This data is represented by a waveform of voltage over time, such as LFP activity.

Let $y_i(t) \in \mathbb{R}$ be the continuous signal associated with the behavior of interest for each trial i, which is typically time locked to some event (e.g., movement onset). Each behavioral signal consists of T_i time bins, which may vary from trial-to-trial.

2.2 Spectral decomposition

The first part of the analysis is dedicated to realizing the temporal singular vectors associated with the largest modes of the time-frequency representation corresponding to the $\mathbf{x}_{ij}$ using SVD, as outlined in Fig. 1b.

2.2.1 Spectral analysis

Spectral analysis is defined as the study of time series in the time-frequency domain. It is performed on the raw neural activity $\mathbf{x}_{ij}$ of each brain region j for each trial i. One can compute the time-frequency spectrum of $\mathbf{x}_{ij}$ to capture the neural oscillations using a variety of approaches (Kass et al. 2014; van Vugt et al. 2007). For details on our preprocessing steps, see Section 3.1.1.

Regardless of the specifics, the result will be the set $\{\mathbf{X}_{ij}\}_{i,j=1}^{I,J}$, where each element $X_{ij}(t, f) \in \mathbb{R}$ is the spectral power associated with time bin t and frequency bin f for brain region j during trial i.

2.2.2 Singular value decomposition

A standard strategy for probing multivariate data is to constrain the complexity of the data. Here, we utilize SVD on $\mathbf{X}_{ij}$ to find the top modes, each with an associated time-component vector and frequency-component vector.

Formally, the equation for SVD is as follows:

$$\mathbf{X}_{ij} = \mathbf{U}_{ij}\, \mathbf{S}_{ij}\, \mathbf{V}_{ij}^T,$$

where $\mathbf{X}_{ij}$ is an $T_i \times F$ matrix containing the original neural spectral data of real values; $\mathbf{U}_{ij}$ is an $T_i \times T_i$ orthogonal matrix known as the left singular matrix; $\mathbf{V}_{ij}^T$ is the transpose of $\mathbf{V}_{ij}$, which is an $F \times F$ orthogonal matrix known as the right singular matrix; $\mathbf{S}_{ij}$ is an $T_i \times F$ rectangular matrix with singular values along the pseudo-diagonal (Gentle 2017). The singular values are nonnegative real numbers, where mode m is denoted $\sigma_{ij,m}$, which are ordered from largest to smallest. The number of nonzero singular values corresponds to the rank of $\mathbf{X}_{ij}$. That is, $M_{ij} = \text{rank}(\mathbf{X}_{ij})$.

SVD is used to decompose $\mathbf{X}_{ij}$ into a linear summation of M_{ij} rank-1 matrices, illustrated in Fig. 2. Specifically:

$$\mathbf{X}_{ij} = \sum_{m=1}^{M_{ij}} \mathbf{A}_{ij,m} = \sum_{m=1}^{M_{ij}} \sigma_{ij,m}\, \mathbf{u}_{ij,m}\, \mathbf{v}_{ij,m}^T, \tag{1}$$

where $\mathbf{A}_{ij,m}$ is an $T_i \times F$ rank-1 matrix composed of the m-th SVD components, or mode m, including the m-th singular value and the left and right singular vectors from the m-th columns of $\mathbf{U}_{ij}$ and $\mathbf{V}_{ij}$, respectively denoted as $\mathbf{u}_{ij,m}$ and $\mathbf{v}_{ij,m}$ (Gentle 2017). Each mode is a unique low-rank approximation. In fact, the best rank-1 approximation of $\mathbf{X}_{ij}$ in terms of minimizing the 2-induced matrix norm is $\mathbf{A}_{ij,1}$ where $m = 1$. Adding the matrix $A_{ij,2}$ to $A_{ij,1}$ would produce the best rank-2 approximation and so on.

2.2.3 Select number of modes

Each $\mathbf{A}_{ij,m}$ will contain unique information about $\mathbf{X}_{ij}$. One can also think of each mode as capturing a unique pattern found in the original spectrogram. Therefore, it may be beneficial to analyze multiple modes. On the one hand, using the first mode may bias the tool to focus its approximation to one particular frequency. On the other hand, one could choose to examine *all* of the modes but this would be computationally expensive and could produce results that are as overwhelming as the original data set.

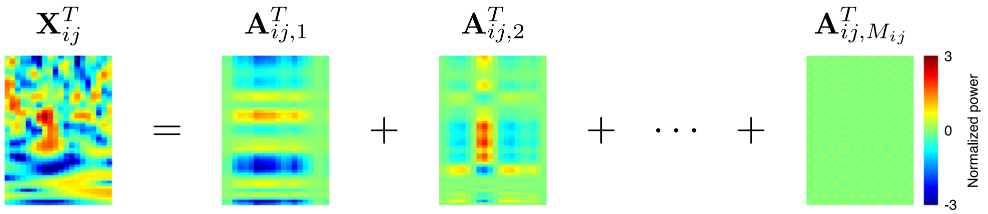

Fig. 2 *SVD*. Example of SVD on a spectrogram. As illustrated above, the spectrogram $\mathbf{X}_{ij}$ can be decomposed into a linear summation of M_{ij} rank-1 matrices as in Eq. (1). Each $\mathbf{A}_{ij,m}$ matrix adds more information about the original matrix, where mode $m = 1$ contains the most information and mode $m = M_{ij}$ contains the least. The transpose of $\mathbf{X}_{ij}$ and $\mathbf{A}_{ij}$ are plotted in the spectrogram so that time is along the horizontal axis and frequency is along the vertical axis

To minimize the number of modes while maximizing the approximation of the original data, one would need to look no further than the largest consecutive modes. The quality of how well $\mathbf{A}_{ij,m}$ reflects the original spectrogram is calculated using the following ratio:

$$R^2_{ij,m} = \frac{\left\| \sigma_{ij,m}\, \mathbf{u}_{ij,m}\, \mathbf{v}^T_{ij,m} \right\|^2}{\left\| \mathbf{X}_{ij} \right\|^2} = \frac{\sigma^2_{ij,m}}{\sum_{m=1}^{M_{ij}} \sigma^2_{ij,m}}. \qquad (2)$$

This quantity is referred to as the amount of variance explained by mode m. Notice how the ratio only depends on the singular values. That is, the squared singular values are proportional to the amount of variance explained by its corresponding singular vectors. The amount of variance explained by each mode for trial i and brain region j can be collated into the vector $\mathbf{R}^2_{ij} \in \mathbb{R}^{M_{ij}}$.

We can use $\mathbf{R}^2_{ij}$ to determine the minimal number of modes to analyze while maximizing the amount of variability across all trials and all brain regions. To find this number, the cumulative sum of $\mathbf{R}^2_{ij}$ is averaged across all trials and all brain regions, appending `NaN` to the end of the vector to match the length of the largest M_{ij}. Alternatively, one could truncate the vectors to an agreeable length.

Figure 3 demonstrates the average cumulative percent of variance explained over the top five modes using our data set described in Section 3. One should immediately observe that most of the variance is explained by the top two modes, which supports the rationale of limiting the analysis to the first few modes.

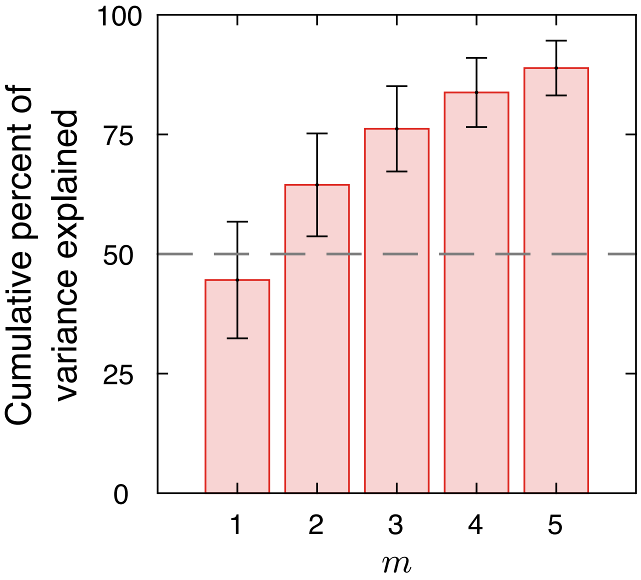

Fig. 3 *Select number of modes.* Plot of the average cumulative percent of variance explained for modes $m \in \{1, \ldots, 5\}$ across all trials and all brain regions. Error bars represent ±1 standard deviation. Notice how the average first mode accounts for nearly 50% of the original data. A criterion can be set to optimize the minimum number of modes needed to maximize the amount of variance captured. For example, the optimal number of modes needed for a criterion of 50 (dashed line)—to capture at least 50% of the variance of the original data—would be $M = 2$

The user can choose a criterion between 0–100% to initiate a constraint that limits the number of modes the tool will analyze. For example, choosing a criterion of 50 would use the minimum number of modes needed to explain at least 50% of all the variance in the original data, which optimally would be the first few modes. We applied this criterion (dashed line in Fig. 3) to our data to find that we only need to use the first 2 modes. The subset of modes the tool will analyze will be denoted as $m \in \{1, \ldots, M\}$ where M is the optimal number of modes based on the criterion.

2.3 Cross-correlation analysis

Next, we aim to relate the temporal summary of neural activity with the dynamic behavioral signal utilizing cross-correlation.

2.3.1 Cross-correlate

To compare the neural activity in brain region j to behavior, we cross-correlate the temporal singular vector $\mathbf{u}_{ij,m}$ and time-varying behavioral signal $\mathbf{y}_i$ for each trial i. The cross-correlation value, or *correlation*, measures the similarity between two signals as a function of lag d. The result is a vector of correlations for each lag value, denoted $\mathbf{r}_{ij,m} \in \mathbb{R}^{2T_i-1}$ (Fig. 1c). Corresponding to each correlation is a p-values, denoted $\mathbf{p}_{ij,m} \in \mathbb{R}^{2T_i-1}$.

2.3.2 Calculate norm

This step measures the strength of the correlation between the two signals by summarizing $\mathbf{r}_{ij,m}$. The p-norm is calculated to measure the "size" of $\mathbf{r}_{ij,m}$ or the overall magnitude of its values. The resulting scalar is denoted as $r_{ij,m}$ and is used to quantify the overall correlation between the two signals for brain region j and trial i. Three common norms are $p = 1, 2, \infty$ (Gentle 2017). Regardless of the type of norm, the result is a scalar $r_{ij,m}$ which quantifies the fit between $\mathbf{u}_{ij,m}$ and $\mathbf{y}_i$.

We commonly choose the infinity norm as our measurement. The infinity norm is a special case whose solution is the maximum absolute value of $\mathbf{r}_{ij,m}$. This choice permits access to alternatively quantifying the strength of the correlation with $p_{ij,m} = \mathbf{p}_{ij,m}(d)$ such that lag d satisfies

$$\|\mathbf{r}_{ij,m}\|_\infty = \max_{-T_i \leqslant d \leqslant T_i} \left\{ |r_{ij,m}(d)| \right\}.$$

Both $r_{ij,m}$ and $p_{ij,m}$ measure the correlation between the approximate neural activity of mode m in brain region j and the behavior for trial i.

2.4 Ranking procedure

Recall that the goal of the analysis is to (i) produce a rank ordered list of pairs of brain regions $j \in \{1, \dots, J\}$ and modes $m \in \{1, \dots, M\}$ sorted by how well neural activity correlates with behavior and (ii) determine a focused range of frequencies that significantly contributes to the neural activity for each of these brain region and modes.

Here, we demonstrate how to accomplish these goals utilizing the results from Section 2.3. The outline of this procedure is shown in Fig. 1d and described below.

2.4.1 Rank ROIs

We define ROIs (Regions-Of-Interest) as the rank ordered list pairs of brain regions and modes sorted from strongest to weakest by the average correlation between the temporal singular vectors and the behavioral signals.

At this point in the analysis, each trial i for brain region j has a correlation for each mode m, denoted $r_{ij,m}$. The decision to make is how to use these values to determine which brain regions are most related to the behavior. There are multiple approaches to summarize the overall relationship between brain region j and the behavioral signal. A straightforward way is to calculate the average correlation for each brain region an mode: $\overline{r}_{j,m} = I^{-1} \sum_{i=1}^{I} r_{ij,m}$. Alternatively, if $p_{ij,m}$ is available, then the average p-value can also be calculated: $\overline{p}_{j,m} = I^{-1} \sum_{i=1}^{I} p_{ij,m}$.

The more closely the temporal singular vector aligns with the behavior signal, the higher the average correlation (or the lower the average p-value) will be. Therefore, these averages can be used to arrange the pairs of brain regions and modes into a rank ordered list, from highest average correlation to lowest average correlation.

Optionally, one could apply a threshold on the averages to limit the number of ROIs to a subset. For example, applying a decision rule of $\theta \leqslant \overline{r}_{j,m}$ grants the user the ability to finely tune a subset of ROIs to those that have an average correlation above θ. Exploring the full list of $J \times M$ ROIs is equivalent to a threshold of $\theta = 0$.

From here, one can freely select a subset of ROIs to further explore, or choose to look at all regions as ROIs.

2.4.2 Rank FOIs

Additionally, a rank ordered list of FOIs (Frequencies-Of-Interest) for a given ROI is found using the frequency singular vectors. The FOIs are obtained by sorting the frequencies which occur from most commonly and influentially across all trials to least. FOIs can be framed in terms of bins or bands.

Recall that $\mathbf{A}_{ij,m}$ can be decomposed into the vectors $\mathbf{u}_{ij,m}$ and $\mathbf{v}_{ij,m}$, where the latter—known as the *frequency singular vector*—summarizes the frequencies that contribute to the m-th mode of $\mathbf{X}_{ij}$. Then it is fair to assume that $\mathbf{v}_{ij,m}$ contains important features pertaining to the contributions of each frequency bin when $\mathbf{u}_{ij,m}$ is strongly correlated with $\mathbf{y}_i$.

The goal of this step is to summarize $\mathbf{v}_{ij,m}$ over all trials by quantifying the influence each frequency bin has on $\mathbf{X}_{ij}$. There are multiple ways to encapsulate $\mathbf{v}_{ij,m}$ over all trials into a $F \times 1$ vector. One approach would be to calculate the average absolute value of each frequency bin across all trials:

$$\overline{\mathbf{v}}_{j,m} = \left\{ \overline{v}_{j,m}(f) = \frac{\sum_{i=1}^{I} |v_{ij,m}(f)|}{I} \right\}_{f=1}^{F} .$$

Frequency bins would be equally weighted across trials since each $\mathbf{v}_{ij,m}$ is a unit vector from the orthogonal matrix $\mathbf{V}_{ij}$. Hence, one could add a weighting factor on $\mathbf{v}_{ij,m}$ to accentuate the response for stronger trials in the average by using correlation value $r_{ij,m}$ or singular value $\sigma_{ij,m}$. For the purposes of this paper, we only considered the nonweighted average.

The FOIs for the m-th mode of brain region j are determined by sorting the values of $\overline{\mathbf{v}}_{j,m}$, from highest to lowest, and reordering the frequency bins along the sorted dimension. In other words, the frequency bins that have the highest absolute average must be the frequency bins that are most influential in $\mathbf{X}_{ij}$. Refer to Section 4 for a discussion on other possible approaches to locating bins of interest.

Above, FOIs are defined using frequency *bins*. But FOIs can analogously be interpreted using the frequency *bands* commonly referenced in literature. Here, we demonstrate one approach with the bands delta (1–4 Hz), theta (4–8 Hz), alpha (8–15 Hz), beta (15–30 Hz), low gamma (30–60 Hz), high gamma (60–100 Hz), and hyper gamma (100–200 Hz) (Basar et al. 2000; Canolty and Knight 2010; Crone et al. 1998a, b; Kahana et al. 2001). The frequency band version of FOIs is found by averaging the aggregated list of frequency singular values for all the bins contained in the band, then ranking each band in a similar manner as before.

3 A motor control case study

We recently collected a data set consisting of neural activity from nonmotor brain regions during a movement task without any predefined hypothesis (Breault et al. 2017; Kerr et al. 2014, 2017). Due to the inherent complexity of human data, we were uncertain as to whether any neural correlates existed between the neural data and path-related behavioral information because no regions within the motor circuit were recorded. Only associative cortices and subcortical structures were accessible. Therefore, we required an exploratory data analysis methods, such as that proposed here, to reveal what brain areas, if any, were relevant to behavior. Analyses on electrophysiological and behavioral data were conducted offline using custom MATLAB® scripts (Mathworks, Natick, MA).

3.1 Neural data

Electrophysiological data were collected from a medically refractory epileptic subject at Cleveland Clinic while performing a motor task. LFP recordings of deep to peripheral brain regions were captured using SEEG technique from multiple depth electrodes implanted for seizure localization (González-Martínez et al. 2015).

Neural recordings were collected at a sampling rate of 2 kHz using a clinical electrophysiology acquiring system (Nihon Kohden 1200, Nihon Kohden America, USA) onsite in the Epilepsy Monitoring Unit. The recording session was free of epileptic activity. All electrode contacts were labeled by clinicians according to anatomical location based on postoperative imaging.

3.1.1 Preprocessing

The neural activity was preprocessed using spectral analysis on the voltage data to obtain the data structure described in Section 2.2.1. Oscillatory power was calculated using continuous wavelet transform with a logarithmic scale vector ranging 1–200 Hz and complex Morlet wavelet with $\omega_0 = 6$. Next, we divided the instantaneous power spectral density into overlapping time bins (50%) by using a time window of 100 ms every 50 ms, averaging over each bin. Each 100 ms time bin was labeled using the last temporal index corresponding to that window. Finally, the power of each frequency bin was log normalized over the entire recording session time using the z-score based on the log of the power for each frequency bin fitted to a standard normal distribution.

3.1.2 Neural temporal summarization

The temporal summary of the neuronal activity from each electrode over all trials was found using the proposed method from Section 2.2.2 on the first $M = 2$ modes. In all, our analysis consisted of $J = 62$ brain regions and $I = 98$ trials from a single subject during one recording session.

3.2 Behavioral data

The raw behavioral data comprised of cursor position recorded using a robotic manipulandum from the InMotion ARM Interactive Therapy System (Interactive Motion Technologies, Watertown, MA, USA), which were collected simultaneously with the SEEG data over the entire session.

3.2.1 Motor task

The subject performed a speed and goal directed reaching movements that have been previously described (Breault et al. 2017; Johnson et al. 2014; Kerr et al. 2014). The interface of the task was prepared in MATLAB (Mathworks, Natick, MA) using MonkeyLogic (Asaad and Eskandar 2008; Asaad et al. 2013) and displayed on a computer screen attached to the manipulandum. The task consisted of several epochs, which were distinguishable by the visual stimuli as shown in a timeline of simulated screens in Fig. 4. A window of time between MoveOnset and HitTarget was used for the neural and behavioral signal in our analysis.

3.2.2 Deriving the behavioral signal

The behavioral signal $\mathbf{y}_i$ for each trial was derived using cursor position. This signal, called the *modulation angle* captured the temporal evolution of the correction angle of the cursor's movement. This angle represents the difference between the instantaneous direction of the cursor and the direction of its current position to the target. The larger the modulation angle was, the more off course the subject's movement was from reaching the target. A modulation angle of zero is interpreted as the subject moving directly towards the center of the target.

The raw position data, such as those seen in Fig. 5, was smoothed using a low-pass Butterworth filter with a cutoff frequency of 10 Hz. For trial i, the gradient on the raw position data was used to obtain the instantaneous vector $\mathbf{w}_i$ for each time point. The target vector $\mathbf{z}_i$ always points towards the center of the target of a trial. The modulation angle $\mathbf{y}_i$ was calculated by extracting the projection of the instantaneous vector on to the straight line between the position point and the center of the target.

The modulate angle was calculated as the angle between the instantaneous and target vectors:

$$y_i(t) = \text{sign}([\mathbf{z}_i(t) \times \mathbf{w}_i(t)] \cdot \mathbf{e}_3) \ \text{atan2d} \left(\frac{\|\mathbf{z}_i(t) \times \mathbf{w}_i(t)\|}{\mathbf{z}_i(t) \cdot \mathbf{w}_i(t)} \right)$$

using the four-quadrant inverse tangent in degrees (MATLAB 2017). In our equation, we solved for the magnitude and direction of modulation angle separately. We then combined terms with element-wise multiplication to get a vector of angles between $[-180°, 180°]$ at each time point t for trial i. A visualization of this calculation is demonstrated in Fig. 5. The behavioral signal was subsequently downsampled in order to match the time indexing of the neural signal.

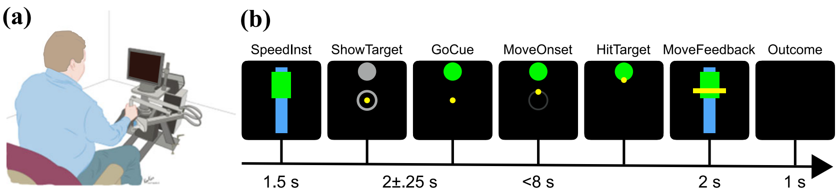

Fig. 4 *Motor task.* **a** An illustration of the manipulandum set-up in relation to the subject, who sat approximately two feet from the screen. **b** A detailed timeline of visual stimuli displayed on the screen over the course of a completed trial. The goal of the task was to move a cursor to the target at an instructed speed. Each trial began with a speed instruction of either "fast" or "slow," represented by the position of the green rectangle on the blue bar (SpeedInst). After the subject moved the yellow cursor to the center, one of four targets was presented (ShowTarget) for 2 ± 0.25 s (mean ± standard deviation) prior to movement command (GoCue). The point when the yellow cursor left the center (MoveOnset) was marked in order to capture the point in the movement that did not include movement initiation (MoveOnset). The movement was complete after the cursor hit the target (HitTarget) and stayed in the target for 0.50 s. The subject received immediate feedback on their trial speed relative to the speed instruction, as represented by the thin yellow rectangle (MoveFeedback). If they successfully met the speed instruction, then a $5 bill was displayed. Otherwise, they were shown a red X (Outcome). The time window chosen for this analysis was between MoveOnset and HitTarget

3.3 Correlation results

The infinity norm ($p = \infty$) was used to capture the absolute maximum correlation, $r_{ij,m}$, and the concurrent p-value, $p_{ij,m}$, between $\mathbf{u}_{ij,m}$ and $\mathbf{y}_i$ across $m \in \{1, \ldots, M\}$, $i \in \{1, \ldots, I\}$, and $j \in \{1, \ldots, J\}$.

To understand the relationship between $r_{ij,m}$ and $p_{ij,m}$, the pairs were organized in a scatter plot seen in Fig. 6a where the points are shaded from short (light) to long (dark) trials. The general trend observed is that higher correlations coincide with lower p-values. Hence, a strongly correlated trial also tends to be a statistically significant trial. There is also a tendency for shorter trials having higher correlations but higher p-values. This is inherently due to the fact that lesser time bins will lead to weaker p-values despite large correlations. The opposite is true for longer trials. These trials will tend to get lower correlation but lower p-values since there are more time bins.

Examples of a weak and strong correlation were prepared in Fig. 6b–c, respectively, to obtain intuition about $r_{ij,m}$. Each example represents a separate brain region during different trials. We first wanted to confirm whether $\mathbf{u}_{ij,m}$ represented the spectrogram well enough before judging the fit of the correlation, via visual inspection.

It is clear that both examples of $\mathbf{u}_{ij,m}$ summarize aspects of their spectrograms. In the weak example (Fig. 6b), the temporal singular vector summarizes rhythmic oscillation across 30–200 Hz while the strong example (Fig. 6c) summarizes the broadband activity across 4–15 Hz and 8–100 Hz. Therefore, $\mathbf{u}_{ij,m}$ is a sufficient representation of

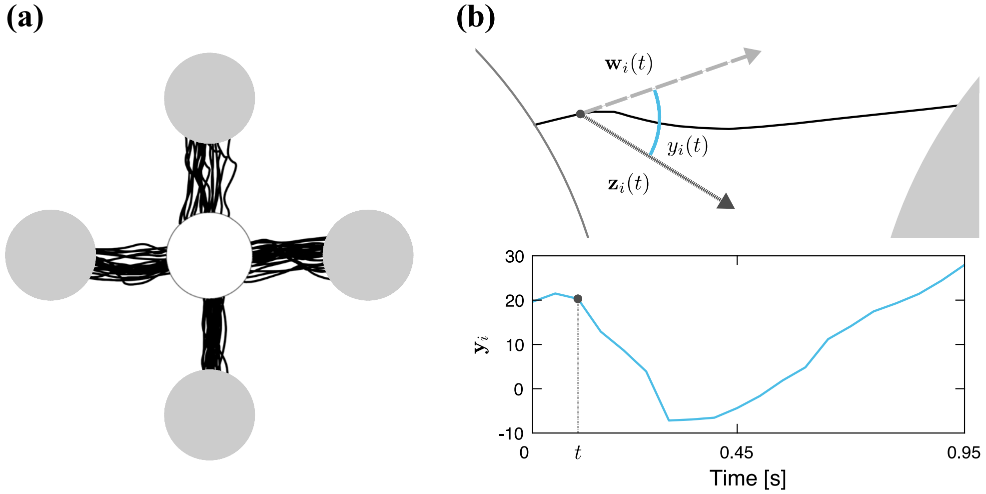

Fig. 5 *Deriving the behavioral signal.* **a** The raw cursor trajectories of 98 trials from one subject used between MoveOnset and HitTarget. This data was used to derive the behavior signal called modulation angle. For each trial, the subject was instructed to move a cursor from the center circle to one of four targets. Cursor paths varied from trial-to-trial. **b** (Top) Visual representation of modulation angle at time point t overlapping actual cursor position for a particular trial i. (Bottom) Plot of $\mathbf{y}_i$ computed from the cursor position moving from the center to the right target. The dot represents the modulation angle measured between $\mathbf{w}_i$ (dashed line) and $\mathbf{z}_i$ (hashed line) at the same corresponding time point t visualized above. The event is time locked to MoveOnset

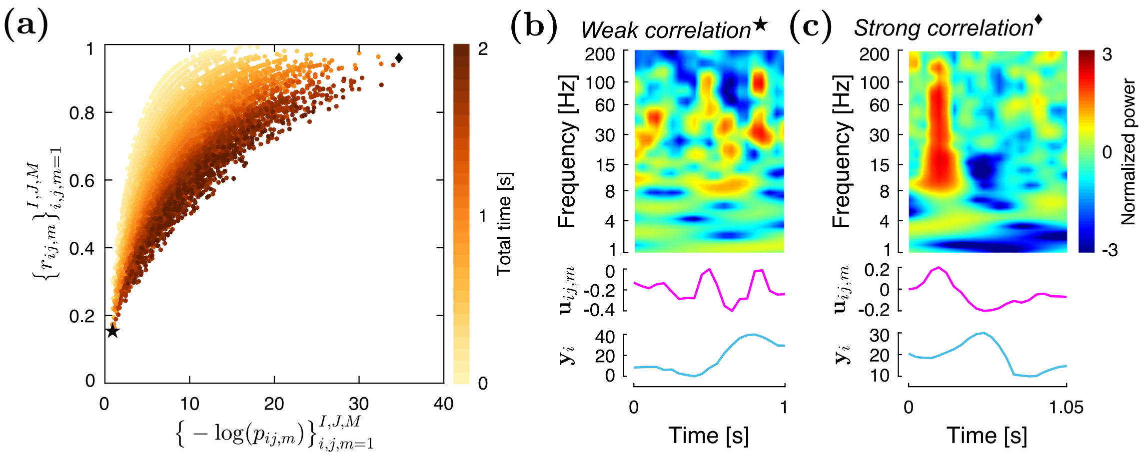

Fig. 6 *Calculate norm.* **a** Scatter plot of $r_{ij,m}$ and associated $p_{ij,m}$ across all trials, brain regions, and modes. The p-values have been transformed for visualization purposes by $-\log(p_{ij,m})$. The number of points depends on the number of trials I, brain regions J, and the number of modes M. In our example, $I = 98$, $J = 62$, and $M = 2$, resulting in $I \times J \times M = 12,152$ total points of $(r_{ij,m}, p_{ij,m})$. Points are colored based on the total time of the trial from short (light) to long trials (dark). **b** The original spectrogram, $\mathbf{u}_{ij,m}$, and $\mathbf{y}_i$ from a weakly correlated example where $(r_{(2,1),1}, p_{(2,1),1}) = (0.16, 0.46)$, marked by the star (★) in the lower left quadrant of the scatter plot in (**a**). **c** The original spectrogram, $\mathbf{u}_{ij,m}$, and $\mathbf{y}_i$ from a strongly correlated example where $(r_{(90,59),1}, p_{(90,59),1}) = (0.96, 8.3 \times 10^{-16})$, marked by the diamond (♦) in the upper right quadrant of the scatter plot in (**a**)

the spectrogram. The strength of the correlation between $\mathbf{u}_{ij,m}$ and $\mathbf{y}_i$ are evident by visual comparison. The temporal singular vector of the weak example has an oscillatory pattern that is not matched by the behavioral signal. Meanwhile, the temporal singular vector of the strong example has a clear positive correlation. From these observations, it is clear to see why Fig. 6b received a low correlation and Fig. 6c received a high correlation.

3.4 Ranking results

Using the results of SVD and cross-correlation, ROIs and corresponding FOIs were ranked as described below.

3.4.1 ROIs

The average correlation $\overline{r}_{j,m}$ for each mode of each brain region was calculated, as discussed in Section 2.4.1. Under this regime, it is assumed that brain regions encoding the behavior will have a higher average correlation than those that are not encoding the behavior. Figure 7a shows the distribution of $\overline{r}_{j,m}$, which was found to have a mean of 0.65 ± 0.03 (mean ± standard deviation) with a negative skewness. This skewness may indicate a subset of highly correlated regions.

Next, brain regions were arranged in a list, ordered by their respective $\overline{r}_{j,m}$ to find the preliminary ROIs. Figure 7b shows a subset of brain regions with the highest $\overline{r}_{j,m}$ (dark left) and the lowest $\overline{r}_{j,m}$ (light right). Interestingly, 9 out of the 10 ROIs were found using the second singular vector.

To verify whether there was a significant difference between correlations from the top ranked ROI compared to the correlations from the bottom ranked ROI, a two-sample t-test was performed using the distributions of $r_{ij,m}$ from the highest and lowest ranking ROI from Fig. 7b. These distributions (Fig. 7c) were found to statistically differ ($p \leqslant 0.05$).

Though we used $\overline{r}_{j,m}$ for demonstrative purposes, similar results are found when using the corresponding $\overline{p}_{j,m}$. The concern brought up in Section 3.3 and Fig. 6a about trial lengths would be nullified if all brain regions are averaged using the same trials. Hence, each average would be equally conflicted by the disparity due to the dependence of p-values and the number of observations in a trial.

Upon closer observation, we determined that the top 10 ROIs shown in Fig. 7b primarily consisted of limbic and visual brain regions (Esslen et al. 2003; Gitelman et al. 1999). In other words, limbic and visual regions of the brain were correlated with our behavioral metric measuring movement error. This preliminary result suggests that the brain could be emotionally reacting to the subject moving their cursor "off course" from the intended target.

The left superior temporal gyrus was found in the both ROIs subsets consisting of the highest and lowest $\overline{r}_{j,m}$. This indicates that some electrode contacts within the same labeled brain region may be observing different neuronal responses, implying that neurons within the same region can simultaneously produce two different signals to generate the same behavior. This is consistent with the idea that the activity within a region is not necessarily ubiquitous,

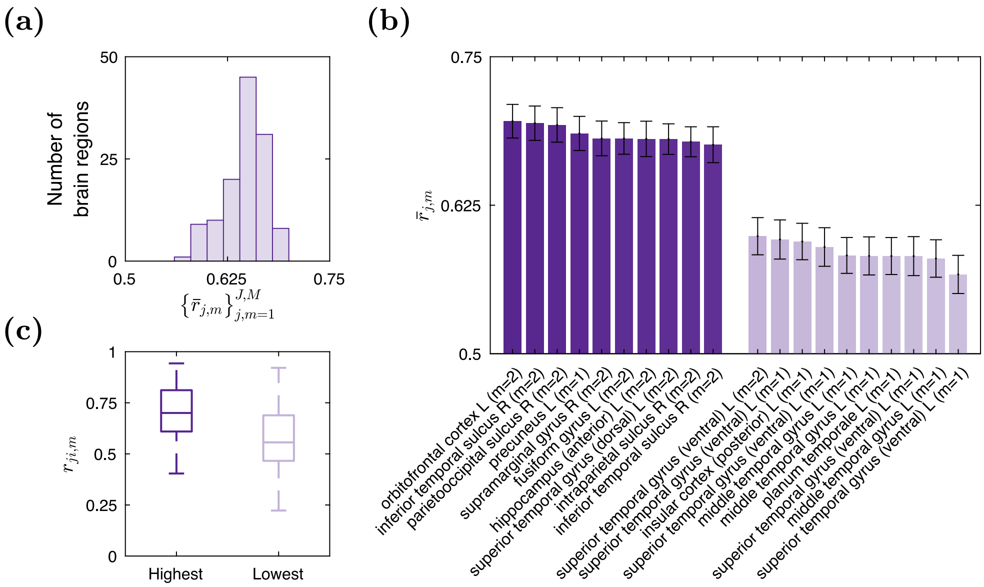

Fig. 7 *Rank ROIs.* **a** Histogram of average correlation $\bar{r}_{j,m}$ across all pairs of brain regions and modes. The mean of the distribution is 0.65 ± 0.03 (mean ± standard deviation) with a negative skew, indicating that more pairs of brain regions and modes have an average correlation above 0.65 than below. **b** Bar graph of a subset of 20 ROIs consisting of the 10 brain region modes with the highest average correlation $\bar{r}_{j,m}$ (dark left) and 10 brain region modes with the lowest average correlation $\bar{r}_{j,m}$ (light right). Error bars represent ±1 standard error of the mean based on the distribution of correlations $r_{ij,m}$ for each brain region j and mode m. **c** Box plot of $r_{ij,m}$ values of the correlations for the brain region and mode pairs with the highest average correlation $\bar{r}_{j,m}$ (dark left) and the lowest average correlation $\bar{r}_{j,m}$ (light right). These distributions were compared using a two-sample t-test and found to be statistically different ($p \leqslant 0.05$)

namely noticed in larger areas such as the superior temporal gyrus. In actuality, the superior temporal gyrus found in the top was located on an electrode located more dorsally to the superior temporal gyrus in the bottom. Further, the left superior temporal gyrus had more electrode contacts than most other regions, consisting of 12.90% of all contacts compared to 1.61% of right precuneus contacts.

For the purposes of this demonstration, we arbitrarily restricted our ROIs to the 10 brain regions with the highest $\bar{r}_{j,m}$, as shown in Fig. 7b and Table 1. However, it is important to emphasize that the ROI decision is entirely defined by the user of this tool.

3.4.2 FOIs

FOIs were found using the frequency singular vector $\mathbf{v}_{ij,m}$ for each ROI as described in Section 2.4.2.

Figure 8a showcases the result of FOI extraction using all trials in the left OrbitoFrontal Cortex (OFC), which happened to be the top ROI in Fig. 7a. The most influential bins ranged primarily between 7–54 Hz. The least significant frequency range was between 100–200 Hz. Table 1 contains the top 24 (out of 55) FOIs in terms of frequency bins of the ROIs, in numerical order.

A common representation of frequency domain on neural data is to group frequency bins into frequency bands. Using the predefined bands and procedure stated in Section 2.4.2, FOIs in terms of frequency bands were found using the same procedure. In Fig. 8b, we found the following bands in order from most to least important: alpha, beta, low gamma, theta, high gamma, delta, hyper gamma. These bands correspond with the ranges found to be most and least important from the frequency bin results described in the paragraph above.

Refer to Table 1 for the top 3 (out of 7) FOIs band of the remaining ROIs, ordered by their frequency range. In Section 3.4.4, we discuss an application for the FOIs based on this example.

3.4.3 Method comparison

This framework is flexible enough to be utilized for a variety of conditions. One could consider omitting spectral decomposition (Section 2.2) in favor of correlating the behavioral signal to the *raw* neural time series. In this section, guided by qualitative examples, we show that skipping spectral decomposition leads to biased correlations and restricts the tool from producing a comprehensive result.

The raw voltage signal was downsampled using the MATLAB function `decimate`. This signal was used as a substitute for $\mathbf{u}_{ij,m}$ to run through the cross-correlation analysis (Section 2.3) and rank ROIs (Section 2.4.1). FOIs could not be calculated due to missing frequency information from the lack of spectral decomposition.

Table 1 List of selected ROIs and FOIs extracted using the proposed tool

ROIs	*m*	Brain regions	FOIs bins [Hz]	FOIs bands
42	2	orbitofrontal cortex L	7–54	alpha, beta, low gamma
24	2	inferior temporal sulcus R	6–13, 16–54	alpha, beta, low gamma
45	2	parietooccipital sulcus R	8–46, 84–109	alpha, beta, low gamma
48	1	precuneus L	1–7, 9–14, 17–21	delta, theta, alpha
60	2	supramarginal gyrus R	5, 10–65, 84	alpha, beta, low gamma
7	2	fusiform gyrus L	4–5, 8–54	alpha, beta, low gamma
12	2	hippocampus (anterior) L	4, 6–46	alpha, beta, low gamma
50	2	superior temporal gyrus (ventral) L	1–6, 8–9, 46–84	delta, theta, high gamma
30	2	intraparietal sulcus R	4, 10–11, 14–84	beta, low gamma, high gamma
25	2	inferior temporal sulcus R	4–6, 8–42	alpha, beta, low gamma

The distribution of average correlation using the raw data (not shown) was symmetrical with a mean of 0.53 ± 0.07, which was lower than the distributions of the spectral correlations (Fig. 7a). Further, the raw correlation results were neither as strong nor as significant as the spectral correlation results. Comparing the correlation scatter plots from the raw analysis (Fig. 9a) to the spectral data (Fig. 6a), the raw correlations are weaker than the spectral correlations as shown by the lack of points in the upper right quadrant. This leads us to believe that the temporal singular vectors correlated better than the raw data to the behavioral data.

We will refer to the ROIs from the raw data as raw ROIs and the ROIs from the spectral decomposition as spectral ROIs. The top 10 raw ROIs consisted primarily of brain regions from the limbic system, including the left cingulate cortex (posterior), left hippocampus (anterior and posterior), right hippocampus (anterior), and left amygdala.

To understand why the tool found correlation using the raw data and the cause of the disparity between the top 10 raw ROIs and spectral ROIs, we qualitatively compared the spectral ($m = 1$), raw, and behavioral data on a trial-by-trial case. We choose to visualize the left hippocampus (anterior). Examples of our tool are exhibited in Fig. 9 for two cases: (b) when the raw data correlated well with behavior and (c) when the raw data did not correlate well.

Upon visualization, it was clear that the high correlation between the raw and behavioral data was obtained due to a bias towards the lower frequency component in the raw signal, which closely matched the low frequency inherent in the behavioral signal. This bias may explain why the top raw ROIs were populated by primarily limbic regions. The limbic system is known for emotional processing and memory, functions that tend to associate with slower waves such as delta and theta (Basar et al. 2000; Kahana et al. 2001; Knyazev 2007). This claim is supported by the FOI

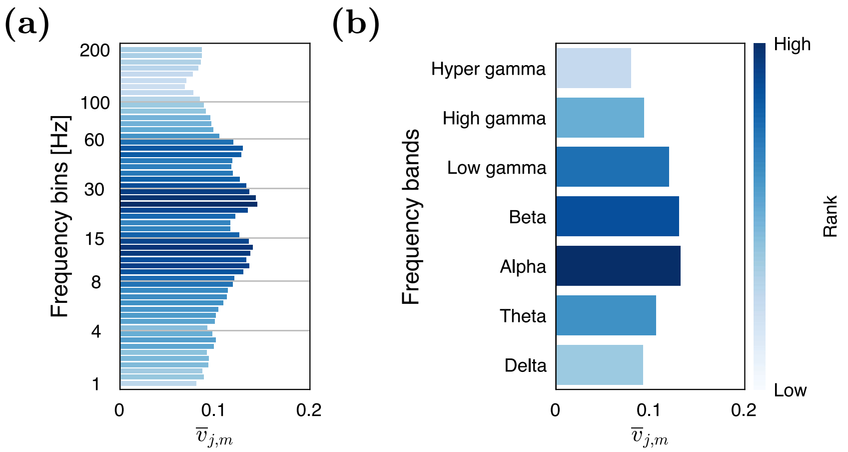

Fig. 8 *Rank FOIs of left OFC.* **a** Bar graph of the average absolute frequency singular vector $\overline{\mathbf{v}}_{j,m}$ for brain region j in frequency bins. Grey horizontal lines represent the bounds for each frequency band. Bars are colored according to their relative ranking, from highest (dark) to lowest (light). **b** Bar graph of the average absolute frequency singular vector $\overline{\mathbf{v}}_{j,m}$ for brain region j in frequency bands according to Section 2.4.2. Bars are colored according to their relative ranking, from highest (dark) to lowest (light)

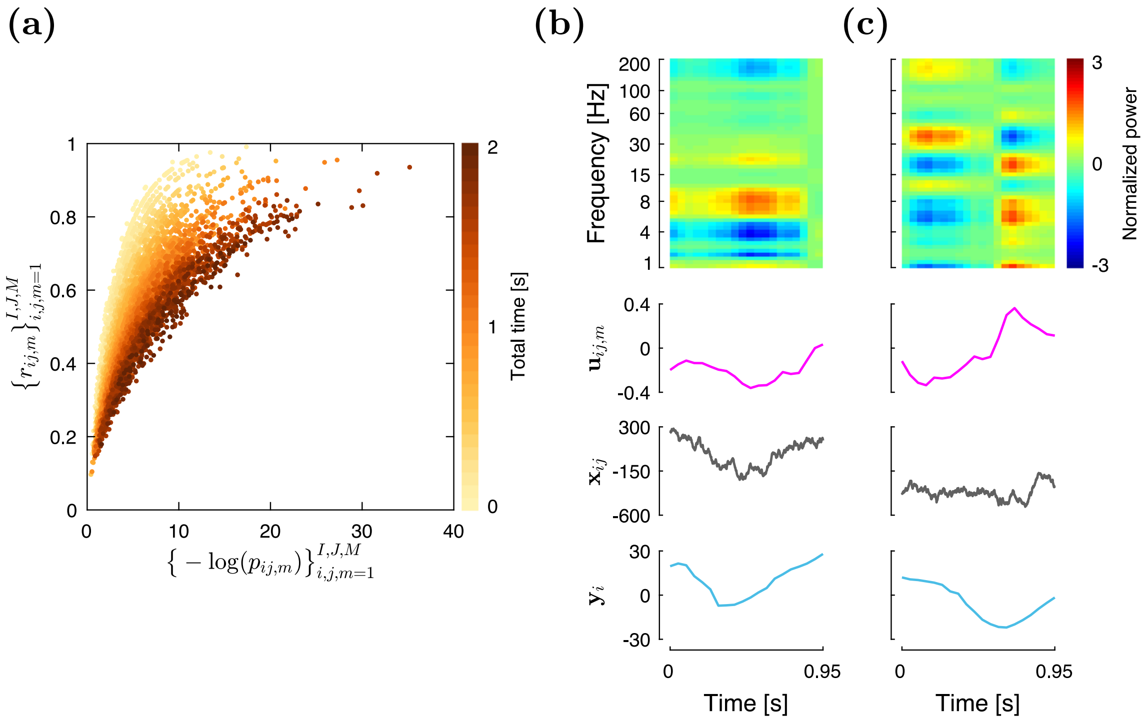

Fig. 9 *Method comparison.* **a** Scatter plot of $r_{ij,m}$ and associated $p_{ij,m}$ by correlating the raw data to the behavioral signal, across all trials and brain regions. The p-values have been transformed for visualization purposes by $-\log(p_{ij,m})$. Points are colored based on the total time of the trial from short trials (light) to long trials (dark). "Good" points are those located in the upper right quadrant, indicating a strong and significant correlation. Correlations found using the raw data were neither as strong nor as significant as the correlations found using the temporal singular vectors seen in Fig. 6a. **b** Example trial of the left hippocampus (anterior) having a high correlation with the behavioral signal for both the raw data $\left(\left(r_{(12,5)}, p_{(12,5)}\right) = \left(0.91, 3.3 \times 10^{-8}\right)\right)$ and spectral data $\left(\left(r_{(12,5),1}, p_{(12,5),1}\right) = \left(0.76, 3.9 \times 10^{-5}\right)\right)$. This follows a similar layout as Fig. 6b–c, with the addition of the raw signal x_{ij} over the same duration. The raw signal and temporal singular vector $u_{ij,m}$ share a similar influence from a lower frequency component that complements the behavioral signal y_i, hence their high correlations. **c** Example trial of the left hippocampus (anterior) with contradicting results between the raw data $\left(\left(r_{(12,27)}, p_{(12,27)}\right) = \left(0.53, 3.8 \times 10^{-3}\right)\right)$ and spectral data $\left(\left(r_{(12,27),1}, p_{(12,27),1}\right) = \left(0.93, 1.9 \times 10^{-10}\right)\right)$ with the same layout. The raw data appears to be composed of higher frequencies relative compared to the behavioral signal. The spectral data is able to capture the frequency components that correlates with the behavioral signal in a way that the raw data could not

bands found for the left hippocampus (anterior) ($m = 1$)—associated with memory processing (Kahana et al. 2001)—which included delta, theta, high gamma, and hyper gamma (not shown).

Therefore, the spectral deposition step retains the essential qualities of the raw data. Moreover, spectral deposition enhances the capability of our proposed tool by providing more comprehensive results, which includes stronger significant correlations and a complete frequency inspection exclusive to SVD via multiple modes and FOIs.

3.4.4 Moving towards confirmatory analysis

This tool could be the first step for numerous applications that a neuroscientist may devise, from preliminary exploratory analysis to trial condition comparisons. This section summarizes two results found by applying the proposed framework to our data set. In particular, we focused on three of the top 10 spectral ROIs: the left OFC (inset Fig. 10a) as well as the left and right precuneus (inset Fig. 10b).

The highest FOI band for the left OFC was the alpha band as shown in Fig. 8b and listed in Table 1. Upon viewing the results of the left OFC on a trial-by-trial case, we observed a modulation in alpha band activity around instances of positive critical points (a.k.a. turning points) in the behavioral signal for left and right trials.

To capture our observation, we summarized the neural activity of each trial into a single scalar by averaging across frequency and time in the original spectrogram using a window around the alpha band (8–15 Hz) and a time-locked window of ±0.2 s corresponding to the time around the positive critical point(s) in the behavioral signal. A simple confirmatory analysis was performed by plotting this average alpha power against the concurrent value of the positive critical point across all left and right trials. The Pearson correlation and corresponding p-value were calculated to quantify the relationship between neural activity and the value of the critical point.

As shown in Fig. 10a, we found a significant ($p \leqslant 0.05$) positive linear relationship between the magnitude of the

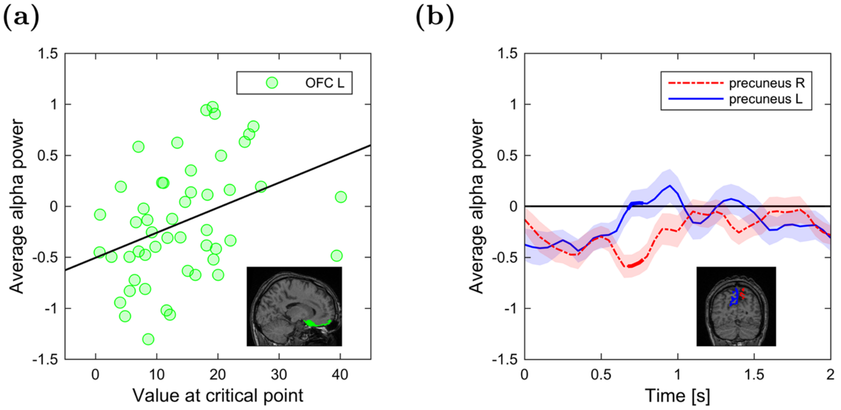

Fig. 10 *Applications.* **a** Scatter plot of average normalized alpha power in left OFC time-locked to positive critical points during left and right trials ($n = 50$). The Pearson correlation and p-value were calculated to find a significant ($p \leqslant 0.05$) positive trend line (solid line) with a slope of 0.37 and p-value of 8.2×10^{-3}. (Inset) Anatomical location of left OFC, highlighted on an MRI slice in matching color. **b** Plot of average normalized alpha power in left precuneus (solid line) and right precuneus (dot-dashed line) over all right trials ($n = 28$) shaded using ±1 standard error and a window time-locked from movement onset at 0 s until 2 s after movement onset. The time-series were compared using a nonparametric cluster statistic. We found a statistical difference ($p \leqslant 0.05$) between 0.5–1 s, indicated by the solid thickened portion on both lines. (Inset) Anatomical location of left and right precuneus, highlighted on an MRI slice in matching colors

critical point and the average alpha power. That is, the larger the critical point, the higher the power in alpha band co-occurs. This observation relates to the functionality of the left OFC in movement planning evaluation. In a previous study of this data by Kerr et al. (2017), OFC activation was observed in trials when random force perturbations were applied to the manipulandum where the magnitude of OFC activation scaled with the force of the perturbation. Bryden and Roesch (2015) found that activity in OFC increased in response to suppressing or redirecting movements. Our observation leads to the hypothesis that OFC is reacting to the subject redirecting their movement due to unexpected drifts, measured by the critical points, scaled by the magnitude of how “off course” they were.

Next, we compared the bilateral functionality of the precuneus, as it was one of the few regions that was recorded in both hemispheres as well as highly ranked. In particular, the left precuneus was the only ROIs in the top 10 that was found using the first mode ($m = 1$). The right precuneus was ranked shortly after (14 out of 124).

We conducted a temporal confirmatory analysis by averaging the alpha band (8–15 Hz) activity in both brain regions over all right trials using their common FOIs band alpha. The temporal signal of each brain region was then compared using a nonparametric cluster statistic to locate times where the signals statistically differed (Breault et al. 2017; Kerr et al. 2017; Sacré et al. 2016). A time window of 2 s after movement onset ensured we were capturing the neural activity for the entirety of all right trials. Using right trials, which had an average trial time of 0.94±0.33 s, we found a significant difference ($p \leqslant 0.05$) between the left (solid line) and right (dot-dashed line) precuneus between 0.5–1 s after movement onset (Fig. 10b).

The approximate anatomical location of the left and right precuneus is shown in the inset of Fig. 10b. Each precuneus began movement onset (0 s) with an initial decrease in neural activity relative to baseline. Roughly 0.5 s after movement onset, the left precuneus returned to baseline while the right precuneus maintained a steady decrease until 1 s. Our finding aids us in developing questions for future studies, such as why is there a disparity between the hemispheres and how does this relate to our behavioral signal.

It is important to emphasize that these observations are just examples of the capability of our tool to aid in forming novel hypotheses and motivating other studies from evidence it finds that may have previously gone unnoticed.

4 Discussion

This methodology is useful for scientists who wish to refine their large-scale spectral neural data into an objective subset of regions and frequencies that correlate with a dynamic task signal for further investigation. Our versatile framework is not only tractable and fast—sifting through our example of whole-brain spectral data in eight seconds—but also provides a multitude of flexibilities: it is robust enough to account for trial-to-trial variability, does not require predefined frequency bands, and adapts to different signals.

Though the use of SVD is not novel, our manner at which we apply it is unique. Correlating time singular vectors, found by decomposing spectral data via SVD, to behavior is novel to our knowledge.

In this paper, we have shown one way this general framework can be applied. Below, we discuss how to modify each step to fit the aim of any analysis.

Since each mode will emphasize a distinctive pattern in the spectrogram (i.e., different phases or frequencies), one may consider utilizing the other singular components and their directions in addition to or instead of the first. One may find regions that originally had weak correlations may actually have strong correlations for a different mode. In this paper, we demonstrated a method by which one could choose and include multiple modes. This type of analysis confirmed that each mode contains unique information, as we found that FOIs using $m = 1$ primarily picked up lower frequency bands, such as delta and theta, whereas FOIs using $m = 2$ picked up relatively higher frequency bands.

In general, the relative magnitude of the power in each spectrogram should be considered when choosing the mode, as some may contain overpowering activity such as broadband bursting, which could drown out any other patterns. Instead of throwing these trials away, one can use SVD to filter out the noise. Extreme activity will be primarily accounted for by the first few modes, meaning the others may contain subtle patterns that may correlate with behavior. It is also good practice to always look at the data before, during, and after any analysis step.

Another variation could be to interchange different dynamic signals, such as physiological or behavioral measurements, or even compare time singular vectors between brain regions. When faced with data littered with confounding variables, or multiple trials conditions, it may be appropriate to probe subsets of the data based on trial conditions. This tool is versatile enough to fit partitions of data, such as specific trial conditions. Our application example was obtained using our tool on a subset of trials consisting of left and right targets. However, this adaptability comes with the disadvantage that it can sometimes be difficult to find commonality in activity within regions or amongst trials.

In addition to the scalability of implementing SVD in MATLAB, the customizability of our methodology is prevalent in every major step. There are five critical decisions users must make: 1) Selecting the number of modes to analyze, 2) Summarizing correlations across trials and regions, 3) Defining the ROI decision rule, 4) Summarizing frequency bins across trials and regions, and 5) Defining the FOI decision rule. In this paper, we have demonstrated one of many ways to define these steps. Apart from designating a different correlation measurement or appointing another ranking policy, one could filter out irrelevant trials by imposing a notion of "significant trials" in order to emphasize stronger correlations and more distinctive frequencies. A threshold can be enforced to restrict the number of ROIs, such as limiting brain regions to those that satisfy $\theta \leqslant \bar{r}_{j,m}$. To summarize frequencies, frequency singular vectors can be weighted, by using singular values or correlation for example, on a trial-by-trial case when averaging to emphasize the bins during stronger trials. Finally, we also suggest fitting Gaussian distributions to the bar graph in (Fig. 8a) to identify FOIs. They would be identified using peak detection, based on an interval around the mean of each distribution to mark the FOIs as bins and converting the mean to FOIs bands.

Spectral analysis on neural data traditionally partition frequencies into predefined frequency bands (Breault et al. 2017; Canolty and Knight 2010; Crone et al. 1998a, b; Kerr et al. 2014; Sacré et al. 2016; Ward 2003). However, this may result in losing key features where frequency bins are split. Further, it has been shown that frequency bands ranges vary between humans (Crone et al. 1998a); the range of frequencies that are considered beta band oscillations for one person may overlap into gamma band range in another person. Therefore, it is more general to keep the frequencies in terms of bins as opposed to grouping bins into bands. In this paper, we have shown how to identify FOIs that preserves the frequency bins by utilizing the frequency singular vector. We could have also extracted FOIs as bins using the extreme values in the $\mathbf{A}_{ij,m}$ matrix to identify frequency bins. Still, frequency bands are typically used in favor of bins because of the lack of strategies for analyzing high-dimensional multivariate data. For this reason, we also demonstrated how to frame FOIs in terms of frequency bands.

One aspect of our method not discussed in this paper is the potential implications of correlation lag, defined in Section 2.3.1. It is possible to recover the value of the lag corresponding to the infinity norm (Section 2.3.2). Intuitively, this lag represents the time delay between the neural and behavioral signal that produces the highest absolute correlation. One could explore the relationship of lag between brain and behavior or define a network hierarchy based on the relative lag between brain regions. Further, the addition of a lag term would enable this conceptual framework to be applicable to other fields of study such as phase synchronization and cross-frequency coupling (Canolty and Knight 2010; Varela et al. 2001).

Acknowledgments This work was supported by NSF EFRI 1137237 to S.V.S., J.G.M., and J.T.G. as well as Kavli Foundation to P.S. In addition, M.S.B. was partially supported by the ARCS Foundation as a Paul Wright Memorial Scholar.

Compliance with Ethical Standards Subject enrollment was completely voluntarily and the subject gave informed consent. Experimental protocols were approved by the Cleveland Clinic Institutional Review Board and the methods were carried out in accordance with the approved guidelines.

Conflict of interests The authors declare that they have no conflict of interest.

References

Agarwal, R., Thakor, N.V., Sarma, S.V., Massaquoi, S.G. (2015). PMV neuronal firing may be driven by a movement command trajectory within multidimensional Gaussian fields. *Journal of Neuroscience*, *35*(25), 9508–9525.

Asaad, W.F., & Eskandar, E.N. (2008). A flexible software tool for temporally-precise behavioral control in Matlab. *Journal of Neuroscience Methods*, *174*(2), 245–258.

Asaad, W.F., Santhanam, N., McClellan, S., Freedman, D.J. (2013). High performance execution of psychophysical tasks with complex visual stimuli in MATLAB. *Journal of Neurophysiology*, *109*(1), 249–260.

Basar, E., Basar-Eroglu, C., Karakas, S., Schurmann, M. (2000). Brain oscillations in perception and memory. *International Journal of Psychophysiology*, *35*(2), 95–124.

Breault, M.S., Sacré, P., Johnson, J.J., Kerr, M., Johnson, M., Bulacio, J., González-Martínez, J., Sarma, S.V., Gale, J.T. (2017). Nonmotor regions encode path-related information during movements. In *Proceedings of the 39th annual international conference of the IEEE engineering in medicine and biology society (EMBC)* (pp. 3339–3342).

Brown, E.N., Kass, R.E., Mitra, P.P. (2004). Multiple neural spike train data analysis: state-of-the-art and future challenges. *Nature Neuroscience*, *7*(5), 456–461.

Bryden, D.W., & Roesch, M.R. (2015). Executive control signals in orbitofrontal cortex during response inhibition. *Journal of Neuroscience*, *35*(9), 3903–3914.

Canolty, R.T., & Knight, R.T. (2010). The functional role of cross-frequency coupling. *Trends in Cognitive Sciences*, *14*(11), 506–515.

Chapin, J.K. (2004). Using multi-neuron population recordings for neural prosthetics. *Nature Neuroscience*, *7*(5), 452–455.

Cong, F., Lin, Q.-H., Kuang, L.-D., Gong, X.-F., Astikainen, P., Ristaniemi, T. (2015). Tensor decomposition of EEG signals: a brief review. *Journal of Neuroscience Methods*, *248*, 59–69.

Crone, N.E., Miglioretti, D.L., Gordon, B., Lesser, R.P. (1998a). Functional mapping of human sensorimotor cortex with electrocorticographic spectral analysis: II. Event-related synchronization in the gamma band. *Brain*, *121*(12), 2301–2315.

Crone, N.E., Miglioretti, D.L., Gordon, B., Sieracki, J.M., Wilson, M.T., Uematsu, S., Lesser, R.P. (1998b). Functional mapping of human sensorimotor cortex with electrocorticographic spectral analysis: I. Alpha and beta event-related desynchronization. *Brain*, *121*(12), 2271–2299.

Cunningham, J.P., & Yu, B.M. (2014). Dimensionality reduction for large-scale neural recordings. *Nature Neuroscience*, *17*(11), 1500–1509.

D'Aleo, R., Rouse, A., Schieber, M., Sarma, S.V. (2017). An input-output linear time invariant model captures neuronal firing responses to external and behavioral events. In *Proceedings of the 39th annual international conference of the IEEE engineering in medicine and biology society (EMBC)* (pp. 970–973).

Esslen, M., Pascual-Marqui, R.D., Hell, D., Kochi, K., Lehmann, D. (2003). Brain areas and time course of emotional processing. *NeuroImage*, *21*(4), 1189–1203.

Gentle, J.E. (2017). *Matrix algebra: theory, computations and applications in statistics*, 2nd edn. New York: Springer.

Gitelman, D.R., Nobre, A.C., Parrish, T.B., LaBar, K.S., Kim, Y.-H., Meyer, J.R., Mesulam, M.-M. (1999). A large-scale distributed network for covert spatial attention: further anatomical delineation based on stringent behavioural and cognitive controls. *Brain: A Journal of Neurology*, *122*(6), 1093–1106.

González-Martínez, J., Bulacio, J., Thompson, S., Gale, J.T., Smithason, S., Najm, I., Bingaman, W. (2015). Technique, results, and complications related to robot-assisted stereoelectroencephalography. *Neurosurgery*, *78*(2), 169–180.

Johnson, M.A., Thompson, S., González-martínez, J., Park, H.-J., Bulacio, J., Najm, I., Kahn, K., Kerr, M., Sarma, S.V., Gale, J.T. (2014). Performing behavioral tasks in subjects with intracranial electrodes. *Journal of Visualized Experiments*, (92), pp. e51947.

Jouvet, M. (1969). Biogenic amines and the states of sleep. *Science*, *163*(3862), 32–41.

Kahana, M.J., Seelig, D., Madsen, J.R. (2001). Theta returns. *Current Opinion in Neurobiology*, *11*(6), 739–744.

Kass, R.E., Eden, U.T., Brown, E.N. (2014). *Analysis of neural data*. Berlin: Springer.

Kerr, M., Kahn, K., Park, H.-J., Thompson, S., Hao, S., Bulacio, J., González-Martínez, J., Gale, J.T., Sarma, S.V. (2014). High frequency activity correlates of robust movement in humans. In *Proceedings of the 36th annual international conference of the IEEE engineering in medicine and biology society (EMBC)* (pp. 4391–4394).

Kerr, M., Sacré, P., Kahn, K., Park, H.-J., Johnson, M., Lee, J., Thompson, S., Bulacio, J., Jones, J., González-Martínez, J., Liégeois-Chauvel, C., Sarma, S., Gale, J. (2017). The role of associative cortices and hippocampus during movement perturbations. *Frontiers in Neural Circuits*, *11*, 26.

Knyazev, G.G. (2007). Motivation, emotion, and their inhibitory control mirrored in brain oscillations. *Neuroscience and Biobehavioral Reviews*, *31*(3), 377–395.

Lewicki, M.S. (1998). A review of methods for spike sorting: the detection and classification of neural action potentials. *Network: Computation in Neural Systems*, *9*(4), R53–78.

MATLAB (2017). Four-quadrant inverse tangent in degrees.

Sacré, P., Kerr, M., Kahn, K., González-martínez, J., Bulacio, J., Park, H.-J., Johnson, M.A., Thompson, S., Jones, J., Chib, V.S., Gale, J.T., Sarma, S.V. (2016). Lucky rhythms in orbitofrontal cortex bias gambling decisions in humans. *Scientific Reports*, *6*, 36206.

van Vugt, M.K., Sederberg, P.B., Kahana, M.J. (2007). Comparison of spectral analysis methods for characterizing brain oscillations. *Journal of Neuroscience Methods*, *162*(1), 49–63.

Varela, F., Lachaux, J.-P., Rodrigues, E., Martinerie, J. (2001). The brainweb: phase synchronization and large-scale integration. *Nature Reviews Neuroscience*, *2*(4), 229–239.

Ward, L.M. (2003). Synchronous neural oscillations and cognitive processes. *Trends in Cognitive Sciences*, *7*(12), 553–559.